The Planetary Science Journal, 6:251 (15pp), 2025 November https://doi.org/10.3847/PSJ/ae1012
© 2025. The Author(s). Published by the American Astronomical Society.
OPEN ACCESS

Differentiation, the Exception, Not the Rule: Evidence for Full Miscibility in Sub-Neptune Interiors

Edward D. Young[1,4], Aaron Werlen[2], Sarah P. Marcum[1], Lars Stixrude[1], and Cornelis P. Dullemond[3]
[1] Department of Earth, Planetary, and Space Sciences, University of California, Los Angeles, CA 90095, USA; eyoung@epss.ucla.edu
[2] Institute for Particle Physics and Astrophysics, ETH Zürich, CH-8093 Zürich, Switzerland
[3] Institut für Theoretische Astrophysik, Zentrum für Astronomie, Universität Heidelberg, D-69120 Heidelberg, Germany
Received 2025 June 29; revised 2025 October 2; accepted 2025 October 3; published 2025 November 4

Abstract

We investigate the consequences of nonideal mixing between silicate, iron metal, and hydrogen for the structures of the cores of sub-Neptunes with implications for super-Earths and perhaps other planets formed by mixtures of silicate melt, iron metal, and significant mass fractions of hydrogen. A method of extrapolating what we know about the miscibility in the three bounding binary systems $MgSiO_3$–H_2, $MgSiO_3$–Fe, and Fe–H_2 to the ternary composition space is used to deduce the phase equilibria of this system at relevant temperature and pressure conditions. We find that while separate silicate and metal phases can exist at shallow depths, the phases become entirely miscible deeper in the cores, thus altering the density structure of the cores. The assumption that the interiors of large rocky planets, either with extant magma oceans beneath H_2-rich envelopes or evolved from such bodies, are composed of a differentiated metal core overlaid by a silicate mantle is inconsistent with our understanding of the phase equilibria of these bodies.

Unified Astronomy Thesaurus concepts: Exoplanets (498)

1. Introduction

Based on the Kepler survey, sub-Neptunes are the most abundant planet type in the Galaxy (e.g., F. Fressin et al. 2013; B. J. Fulton et al. 2017). These bodies have bulk densities, ρ, similar to about 1–3 g cm^{-3} compared with Earth's bulk density of 5.5 g cm^{-3}. Studies of the atmospheres of sub-Neptunes are multiplying rapidly in the age of the James Webb Space Telescope (JWST). However, our understanding of their cores, meaning everything beneath the outer envelope, is necessarily limited. In some senses, we are in a period of discovery for sub-Neptunes that parallels our understanding of the core of the Sun in the 1920s (C. H. Payne-Gaposchkin 1925). We need judicious use of physical chemistry to infer what is beneath the outer veils of these copious planets.

Some interpretations of their low densities relative to compressed rock and metal suggest that sub-Neptunes may be mainly a mixture of roughly equal-mass fractions of rock and water (e.g., J. J. Fortney et al. 2007; L. Zeng et al. 2019). To see this, consider that if a sub-Neptune with a density of 2 g cm^{-3} were to be composed of water, with $\rho = 1$ g cm^{-3}, and a core with a bulk compressed core density of 5.5 g cm^{-3}, similar to that of Earth, it would have a mass fraction of water of about 40%. The sources of this putative water are debated (B. Bitsch et al. 2019). Objects in the Kuiper Belt provide one model. Assuming Pluto is composed of a mix of water ice and chondrite-like rock, it has a mass fraction of water of about 20%, suggesting that Kuiper Belt objects are not sufficiently water-rich to provide the feedstock for the proposed water worlds.

Alternatively, sub-Neptunes may have rocklike, molten, or partially molten interiors beneath hydrogen-rich primary atmospheres (Y. Chachan & D. J. Stevenson 2018). The H_2-rich envelopes in this interpretation must comprise percent levels of the planet masses in order to match their bulk densities (e.g., J. L. Bean et al. 2021). For example, assuming a density for H_2 of 0.1 g cm^{-3}, appropriate for the high pressures and temperatures at the base of the envelopes (e.g., G. Chabrier et al. 2019); a compressed core density similar to that for the whole Earth; and a median sub-Neptune density of 2 g cm^{-3}, the planet would have a H_2 envelope comprising 2.7% of its mass.

The dense envelopes in this case are sufficient to delay cooling of the originally hot planets such that the magma oceans beneath may persist for Gyr timescales, depending on the processes of atmospheric escape attending the evolution of each planet (S. Ginzburg et al. 2016; A. Vazan et al. 2018; J. G. Rogers et al. 2024). This implies that extant magma oceans are present among many, and perhaps even most, sub-Neptunes observed today.

There is some observational support for the magma ocean hydrogen-rich envelope structure for sub-Neptunes. The JWST spectrum for the atmosphere of sub-Neptune K2-18 b (B. Benneke et al. 2019), touted as a water-rich "Hycean" planet (N. Madhusudhan et al. 2020), can be explained by equilibration between a hydrogen-rich envelope and an underlying magma ocean (O. Shorttle et al. 2024). The metal-rich, relatively low-C/O atmosphere of sub-Neptune GJ 3090 b could be attributed to interaction with an underlying magma ocean, although a plausible alternative is that the envelope chemistry has been modified by atmospheric escape (E.-M. Ahrer et al. 2025). The outer envelope of sub-Neptune TOI-270 d also exhibits characteristics that can be explained by interaction with an underlying magma ocean, including a mean molecular weight of 5 ± 1 amu (B. Benneke et al. 2024; L. Felix et al. 2025).

The bulk densities of super-Earths indicate that they are rocky planets with broadly Earth-like bulk densities and negligible atmospheres in terms of mass. A strong case can be made that super-Earths form when some sub-Neptunes lose their dense hydrogen-rich envelopes (J. G. Rogers et al. 2024),

[4] Corresponding author.

Original content from this work may be used under the terms of the Creative Commons Attribution 4.0 licence. Any further distribution of this work must maintain attribution to the author(s) and the title of the work, journal citation and DOI.

leaving behind rocky cores. This leads to the well-known radius gap that separates these two classes of planets (J. E. Owen & Y. Wu 2013; B. J. Fulton et al. 2017; A. Gupta & H. E. Schlichting 2019): super-Earths have radii between >1 and 1.7 $R_\oplus$, while sub-Neptunes range from about 1.9 to 4.0 $R_\oplus$. In this view, super-Earth interiors may be similar to those of sub-Neptunes (J. L. Bean et al. 2021). An important caveat is the prospect for degassing of H_2 from the molten interior of a sub-Neptune as it loses its envelope and cools inexorably below some threshold final equilibration temperature (e.g., J. G. Rogers et al. 2025). While super-Earths appear to evolve from sub-Neptunes, it is not yet clear that they retain all of the properties of sub-Neptune cores.

It has been suggested recently that the interface between sub-Neptune magma ocean cores and H_2-rich envelopes should correspond to a phase change from a supercritical magma ocean composed of silicate and hydrogen to molten silicate and a separate hydrogen-rich phase (S. Markham et al. 2022; E. D. Young et al. 2024). This suggestion redefines the meaning of the magma ocean–envelope interface. More specifically, the binodal (sometimes referred to as a coexistence curve, or solvus) in the $MgSiO_3$–H_2 system in this context corresponds to the temperature at a given pressure where a supercritical mixture of silicate and hydrogen exsolves to form two discrete phases (L. Stixrude & T. Gilmore 2025). Identifying the surface of magma oceans with a first-order phase transition at a binodal underscores the fact that phase equilibria at relevant pressure and temperature conditions can lead to quite different pictures of these planets relative to our familiar reference points in the solar system; sub-Neptunes are not simply scaled-up Earths with primary hydrogen atmospheres (E. D. Young et al. 2024).

Here we investigate the nature of the molten cores of sub-Neptunes and, by inference, the cores of their super-Earth descendants and perhaps even the deep interiors of their warm Neptune and ice giant cousins. In particular, we investigate whether sub-Neptunes likely have iron-rich cores like the terrestrial planets in our solar system. This question is important because it is common to model the cores of these planets as if they differentiated into Fe-rich metal cores (sensu stricto) and silicate mantles (e.g., B. Davenport et al. 2025) based on analogy with the rocky bodies in the solar system. The nature of the cores (sensu lato, everything other than the envelope) is relevant to estimate the masses of the hydrogen-rich envelopes required to explain their bulk densities. The more hydrogen the cores retain, the less the density deficits relative to pure rock can be attributed to the outer envelope (e.g., E. S. Kite et al. 2019; H. E. Schlichting & E. D. Young 2022).

Our paper is structured as follows. In Section 2, we discuss bulk chemical constraints on iron-rich cores for exoplanets in general. In Section 3, we describe the binary mixing relationships that are the basis for our analysis. In this section, we present existing and newly derived binary Gibbs free energy surfaces, and we present three new ab initio molecular dynamics simulations in support of these free energy surfaces. In Section 4, we present our new ternary Gibbs free energy surface based on the binary systems and a convex hull approach for calculating the stable phase equilibria in the ternary system. The resulting ternary phase diagram is presented in Section 5, and implications for the interior structures of sub-Neptunes are discussed in Section 6. Conclusions are presented in the final section.

2. Prospects for Extrasolar Fe-rich Metal Cores

2.1. Bulk Chemistry

A first-order constraint on whether or not sub-Neptunes, as well as other extrasolar rock-rich planets, can harbor metal-rich cores comes from their bulk chemical compositions as inferred by stellar elemental abundance ratios. Correlations between rocky planet bulk densities and the relative abundances of Fe, Mg, and Si in their host stars yield inferred mass fractions of the metal cores of rocky exoplanets in the range of 25%–35% (V. Adibekyan et al. 2021). The assumption that most iron resides in metal is validated by observations of polluted white dwarfs (WDs). The iron concentrations in silicate-dominated materials accreted by WDs indicate that they have intrinsic oxygen fugacities similar to planetary building blocks in the solar system (A. E. Doyle et al. 2019). This in turn suggests that the planets built from these materials could have Earth-like, iron-rich metal fractions (I. L. Trierweiler et al. 2023). There is also some more direct observational evidence for rock–metal differentiation for a body orbiting around a WD. C. J. Manser et al. (2019) reported periodic shifts in emission spectral lines from an accretion disk around a WD that are explained by a remnant metal core of a differentiated planetesimal orbiting within the disk around the WD. The metal-like density of the spherical body has apparently permitted the body to avoid tidal disruption as it orbits so close to the WD. The bodies that pollute WDs are generally agreed to be similar to the largest asteroids in the solar system asteroid belt (M. Jura & E. Young 2014; I. L. Trierweiler et al. 2022). Evidence for iron metal polluting a WD is thus evidence for silicate–metal differentiation at relatively low pressures and temperatures but not under conditions relevant for sub-Neptunes.

2.2. Physical Differentiation

The bulk chemical compositions of extrasolar rocky bodies or their source materials appear to be consistent with the formation of iron-rich metal cores. The issue then becomes whether the physics associated with differentiation and the phase equilibria in the silicate–iron–hydrogen system are such that silicate–metal differentiation occurs in the depths of sub-Neptunes.

There is reason to believe that metal cores are not the norm for sub-Neptunes and possibly not for their super-Earth descendants. Magma oceans beneath dense hydrogen-rich envelopes can persist for 10^9 yr under favorable circumstances (S. Ginzburg et al. 2016; J. G. Rogers et al. 2024). Thermodynamic simulations of the global equilibration between Fe-rich metal, silicate (represented by $MgSiO_3$), and H_2-rich envelopes show that metal should have significant fractions of H, O, and Si (H. E. Schlichting & E. D. Young 2022). As a result, metal droplets with sizes controlled by their integrity against shear stresses can become neutrally buoyant, forestalling formation of a metal core (E. D. Young et al. 2024). Similarly, T. Lichtenberg (2021) concluded that turbulent entrainment of metal droplets is also likely simply because of the great depth of the sub-Neptune or super-Earth magma oceans. While it is important to recognize that complete physical separation between metal and silicate

can be questioned in the case of sub-Neptunes, this is not the focus of this paper.

2.3. Miscibility

The focus of this paper is on the phase equilibria of the $MgSiO_3$–Fe–H_2 system and implications for the phases present in the deep interiors of sub-Neptunes. There is evidence from ab initio molecular dynamics simulations, as well as experiments, that deep in the interiors of sub-Neptune magma oceans, discrete silicate and iron-rich metal phases do not exist. These constraints include the existence of complete miscibility between molten MgO and Fe at temperatures above 7000 K and pressures of 60 GPa (S. M. Wahl & B. Militzer 2015; L. Insixiengmay & L. Stixrude 2025) and extensive solubility along this binary join at lower temperatures and similar pressures (J. Badro et al. 2018); complete miscibility between liquid $MgSiO_3$ and H_2 above about 4000 K at, for example, 4 GPa (L. Stixrude & B. Karki 2005); and a pressure-dependent enhancement in the solubility of H in Fe melt relative to silicate melt (L. Yuan & G. Steinle-Neumann 2020; S. Tagawa et al. 2021). All of these studies point to the possibility that silicate and iron metal are miscible. We test this proposition here.

3. Binary Mixing Models

3.1. General Approach

In a closed system in which the composition of the system, specified by a set of mole fractions x_i for components i, temperature T, and pressure P, are constant, phase diagrams can be constructed by minimizing the molar Gibbs free energy, $\hat{G}$. Gibbs free energy is the relevant Legendre transform of internal energy where the variables of interest are composition, T, and P. We focus on the Gibbs free energy of mixing, $\hat{G}_{\rm mix}$, to determine the number and compositions of phases at specified conditions. Toward this end, we make use of two curves in parameter space that are derived from the free energy of mixing. In a binary composition space, the binodal is the loci of compositions for two coexisting stable phases. The spinodal lies interior to the binodal and is the region in composition–T–P space where spontaneous transformation from one phase to two phases is predicted. Between these curves is a region of metastability where two phases may have metastable compositions. One can think of the spinodal as defining the region in parameter space where two phases are assured and the binodal as separating the regions of one-phase and two-phase stability at thermodynamic equilibrium.

3.2. $MgSiO_3$–H_2 System

L. Stixrude & T. Gilmore (2025) explored the nonideal mixing between $MgSiO_3$ and H_2 using density functional theory molecular dynamics (DFT-MD) simulations, including relevant thermodynamic parameters. They find that the system becomes entirely miscible at temperatures greater than approximately 4000 K at relevant pressures. There is a negative dependence of the peak temperature for the crest of the binodal on pressure. The crest of the binodal (solvus) is near 3000 K at 10 GPa and 4000 K at 2 GPa. We adopt their subregular mixing model without modification. Their fit to their DFT-MD simulations yields the free energy of mixing

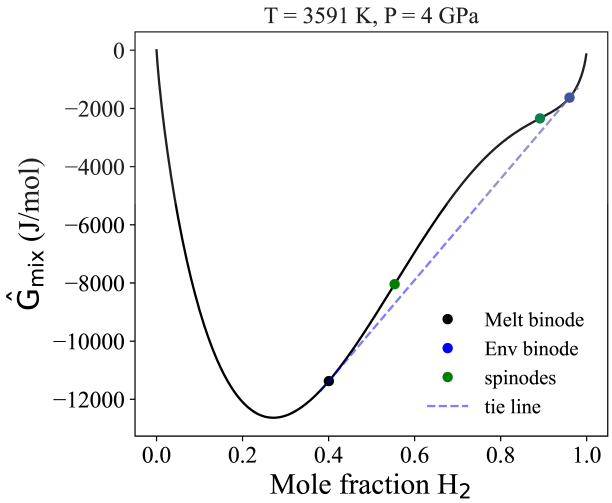

Figure 1. The Gibbs free energy of the mixing surface for the $MgSiO_3$–H_2 system at 3591 K and 4 GPa as formulated by L. Stixrude & T. Gilmore (2025). The binodes for the melt and envelope phases at this T and P, as well as the tie line between them, are shown for clarity. Also shown are the positions of the spinodes where the curvature is zero.

expression

$$\Delta\hat{G}_{\rm mix} = (L_{\rm CB}x + L_{\rm BC}(1-x))x(1-x)\left(1 - \frac{T}{\tau} + \frac{P}{\pi}\right) + RT(x\ln x + (1-x)\ln(1-x)). \quad (1)$$

Here, $L_{\rm CB}$ and $L_{\rm BC}$ are the binary interaction parameters, where the logic for the labels CB and BC will be apparent when we apply these to our ternary model and x is the mole fraction of H_2 along the binary join. In this formulation, the excess, or nonideal, molar enthalpy of mixing is $\Delta\hat{H}_{\rm excess} = (L_{\rm CB}x + L_{\rm BC}(1-x))x(1-x)$. The temperature and pressure dependence for the nonideal mixing is embodied by excess entropy and volume parameters, represented by τ and π, that are $\Delta\hat{H}_{\rm excess}/\hat{S}_{\rm excess}$ and $\Delta\hat{H}_{\rm excess}/\Delta\hat{V}_{\rm excess}$, respectively (L. Stixrude & T. Gilmore 2025). The values for the subregular solution fit to the DFT simulations are $L_{\rm CB} = 62{,}2000$ J mol^{-1}, $L_{\rm BC} = -4950$ J mol^{-1}, $\tau = 4800$ K, and $\pi = -35$ GPa.

The $MgSiO_3$–H_2 system can be used to illustrate the various aspects of the free energy of mixing that we make use of here. The Gibbs free-energy-of-mixing surface for this binary system at 3591 K and 4 GPa is shown in Figure 1. The binodes and spinodes are indicated. In Figure 2, we show the isobaric phase diagram derived from this free energy surface at different temperatures, where the complete binodal and spinodal curves are derived from points at a range of temperatures like those shown in Figure 1 for one temperature.

Here we present two new DFT-MD simulations that bracket the position of the binodal (Figures 3 and 4) as a check on the veracity of the model and an illustration of the two-phase mixing calculations. Methods for the DFT-MD calculations are described in Appendix A. The initial condition for these simulations is composed of two distinct, adjacent phases, $MgSiO_3$ melt and H_2 gas, at the same temperature and about the same pressure (within about 5%). The hydrogen in each case comprises 4% by weight of the system, corresponding to a

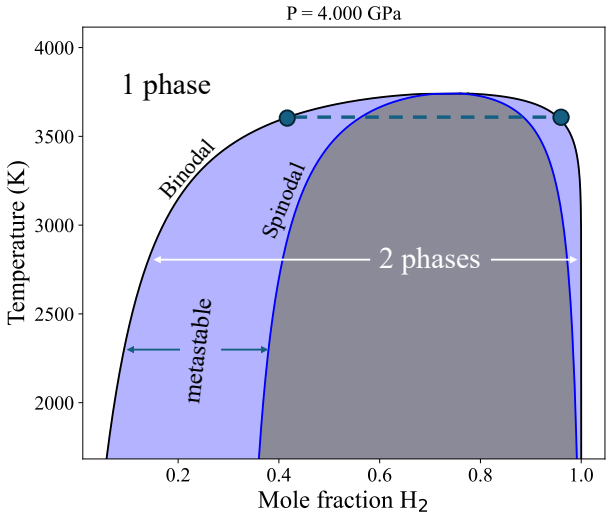

Figure 2. Isobaric phase diagram for the $MgSiO_3$–H_2 binary system as determined by L. Stixrude & T. Gilmore (2025). The one- and two-phase regions outside and inside of the binodal are indicated. A region of metastable compositions for two coexisting phases exists between the binodal and spinodal curves. The compositions of two stable phases at approximately 3600 K are shown by way of example with a dashed tie line connecting them.

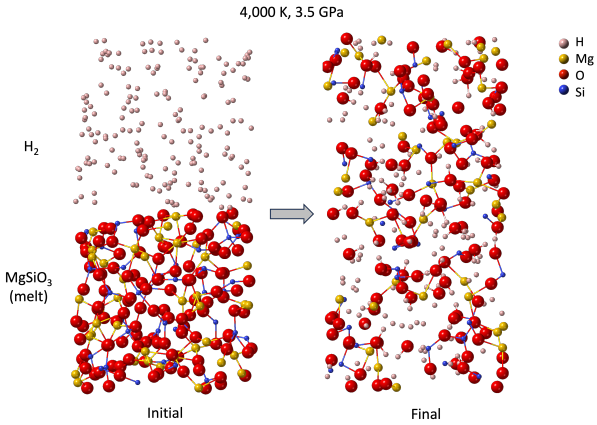

Figure 3. Images of initial and final conditions for the H_2–$MgSiO_3$ system illustrating complete miscibility at 4000 K and 3.5 GPa. The initial condition is composed of $MgSiO_3$ melt overlaid by H_2 gas. The final state is after 13.5 ps of model time. See Appendix B for details.

composition near the peak of the binodal. After suitably long simulation times of >13 ps, the results show that the silicate–H2 system is completely miscible at 4000 K and 3.5 GPa (Figure 3) but not at 3000 K and 2.5 GPa (Figure 4), where the different pressures were used to preserve the number of atoms and volumes for the two different temperatures. This shows that the implied T and P for the binodal for this bulk composition are indeed near those expected for sub-Neptunes with of order a few weight percent H_2.

3.3. $MgSiO_3$–Fe System

There are two published studies showing that molten MgO and Fe become completely miscible at temperatures and pressures relevant for the interiors of sub-Neptunes. S. M. Wahl & B. Militzer (2015) used DFT molecular dynamics calculations and showed that at low pressures, the closure of the binodal (solvus) can occur at temperatures as

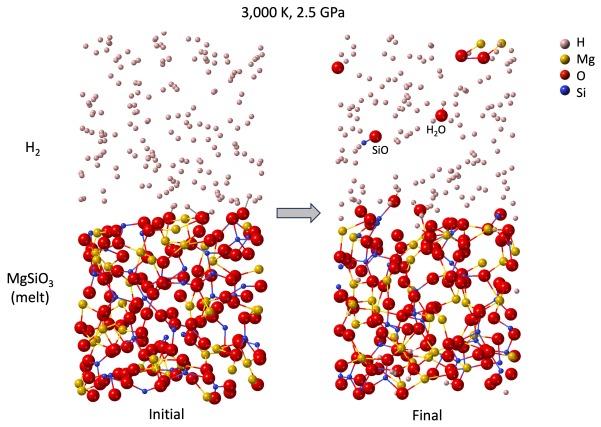

Figure 4. Images of initial and final conditions for the $MgSiO_3$–H_2 system illustrating immiscibility at 3000 K and 2.5 GPa. The initial condition is composed of $MgSiO_3$ melt overlaid by H_2 gas. The final state is after 16.5 ps of model time. Example SiO and H_2O molecules in the gas phase that persist for significant intervals of model time are labeled.

low as 4000 K with a positive pressure dependence. The nonideal mixing is slightly asymmetrical, with the crest of the binodal being about 6000 K at 50 GPa, 7000 K at 100 GPa, and 9000 K at 400 GPa.

More recently, L. Insixiengmay & L. Stixrude (2025) used DFT molecular dynamics to show that liquid MgO and Fe become completely miscible above a temperature of 7000 K at a pressure of 60 GPa and above 9000 K at 145 GPa. These authors fit their simulations to a regular (symmetric) solution model. Their model can be represented as

$$\Delta \hat{G}_{\rm mix} = L_{\rm AC}(T, P)x(1-x) + RT(x\ln x + (1-x)\ln(1-x)), \quad (2)$$

where $L_{\rm AC} = L_{\rm CA} = 240{,}000 - 28T(\rm K) + 1116P(\rm GPa)$ (J mol^{-1}).

To our knowledge, there are no published analogous mixing calculations for $MgSiO_3$–Fe. Nonetheless, it is reasonable to infer that there is nonideal mixing along this join, as in the case of MgO–Fe, and that there is a well-defined binodal that closes at sufficiently high temperatures and pressures.

We performed DFT-MD simulations of the $MgSiO_3$–Fe system in order to test whether the regular solution model for MgO–Fe mixing can be used as a surrogate for the $MgSiO_3$–Fe system at high T and P. Details of the calculations are presented in Appendix A. The results show that at conditions above the MgO–Fe binodal, $MgSiO_3$ and Fe are indeed completely miscible (Figure 5).

There is experimental support for the miscibility of $MgSiO_3$ and Fe at high T and P. J. Badro et al. (2018) observed that the mole fraction of Fe in metal equilibrating with silicate at 4000 K and 54 GPa is only 0.65, with the remainder of the metal phase composed of Mg, Si, and O in roughly 1:1:3 proportions. Similar results were obtained for Fe, Si, Mg, and O by A. Shakya et al. (2024) using machine learning methods for molecular dynamics simulations at 3000–4000 K and 30–35 GPa. This level of mutual solubility at these temperatures and pressures is in reasonable agreement with the DFT calculations.

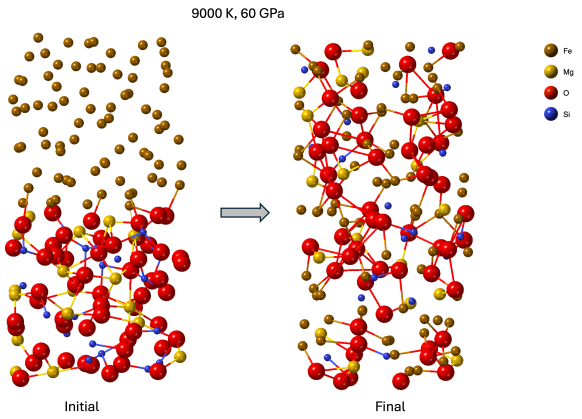

Figure 5. Images of initial and final conditions for the $MgSiO_3$–Fe system illustrating complete miscibility at 9000 K and 60 GPa. The final state is after 7 ps of model time. Time steps were 0.5 fs. The model consists of 76 Fe atoms, 18 Mg atoms, 18 Si atoms, and 54 O atoms.

3.4. Fe–H_2 System

Constraints on the thermodynamics of mixing between Fe and H_2 at relevant T and P come from experiments and ab initio modeling. At relatively low temperatures and pressures (e.g., 2000 K, 0.1 GPa), iron-rich melt coexists with H_2 gas (A. San-Martin & F. Manchester 1990). There is, however, both experimental and modeling evidence that the solubility of H_2 in liquid iron rises sharply at high T and P. S. Tagawa et al. (2021) performed experiments measuring the distribution coefficient for H in molten Fe metal relative to H in molten silicate, $D_H = [H]_{metal}/[H]_{silicate}$, from 3100 to 4600 K and 30 to 60 GPa. They found that while D_H is near unity at $T < 3000$ K, it increases to 10 at 3000 K and 30 GPa and to 30 at 4000 K and 60 GPa. Similarly, L. Yuan & G. Steinle-Neumann (2020) performed ab initio modeling showing that D_H increases from near unity at 0 GPa to about 100 at 40 GPa. These observations all point to an enhancement in the solubility of H_2 in molten Fe metal with pressures greater than about 10 GPa. The requirement for progressive closure of the miscibility gap between H_2 and liquid iron with pressure (Y. Fukai 1992) and the relative distribution of H between molten silicate and iron (increasing D_H) permit a rough calibration of the Fe–H_2 mixing relations.

An additional constraint comes from the parameterization of the solubility of H in molten Fe at lower temperatures and pressures. The compilations by H.-W. Zhang (2007) and G. Jiang et al. (2011) yield the expression

$$\ln(x_H) = -4.423 - \frac{4009\ \mathrm{K}}{T} + \frac{1}{2}\ln\left(\frac{P_{H2}}{1}\mathrm{bar}\right). \quad (3)$$

We make use of this equation as a constraint on the Gibbs free energy surface for mixing of molten Fe and H_2 by matching the melt limb of the binodal to the solubility expressed by Equation (3) at conditions appropriate for our fiducial sub-Neptune magma ocean H_2-rich envelope interface (the minimum required extrapolation of T and P).

We find that all of these relationships are reproduced using a subregular solution model where the interaction parameters are pressure-dependent. The model is

$$\Delta\hat{G}_{mix} = (L_{AB}x + L_{BA}(1-x))x(1-x) + RT(x\ln x + (1-x)\ln(1-x)), \quad (4)$$

where $L_{AB} = 138{,}000–9500P(\mathrm{GPa})\ \mathrm{J\,mol^{-1}}$, $L_{BA} = 17{,}000–9500P(\mathrm{GPa})\ \mathrm{J\,mol^{-1}}$, and x is the mole fraction of H_2 on the binary join. The resulting isobaric phase diagram at 4 GPa is shown in Figure 6. While the precise values used here are certainly not unique, the general shape of the free energy of the mixing surface is required by the observations described above.

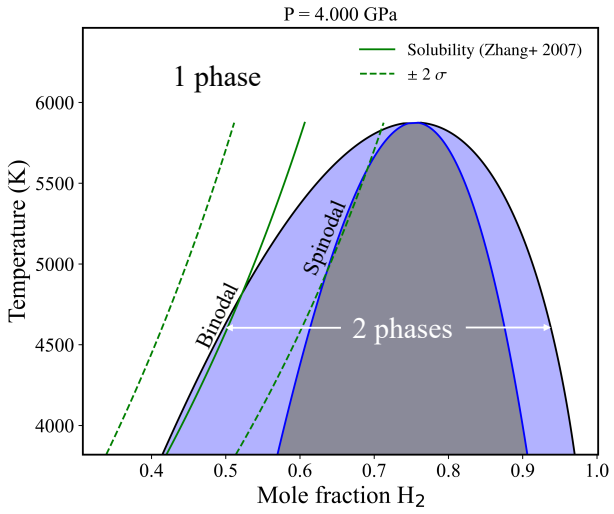

Figure 6. Isobaric phase diagram for the Fe–H_2 binary system based on Equation (4). The extrapolation of the low-P and low-T hydrogen solubility in liquid Fe metal is shown for comparison (H.-W. Zhang 2007; G. Jiang et al. 2011). Errors for the latter are derived by standard propagation of uncertainties.

4. Ternary Mixing Model

We calculate the topology of the Gibbs free energy of mixing in the ternary system $MgSiO_3$–Fe–H_2 as the basis for our analysis. We make use of the mixing models for the three binary systems $MgSiO_3$–H_2, Fe–H_2, and $MgSiO_3$–Fe and extrapolate these bounding binary mixing models into the ternary system. There is a long history of performing such extrapolations with success with percent levels of accuracy (K. Wohl 1946, 1953; Y. Muggianu et al. 1975; K. T. Jacob & K. Fitzner 1977; S. K. Lee & S. J. Kim 2001). We adopt the Muggianu–Jacob method of projecting along the shortest distances from each of the binaries to any given point in the ternary system (Y. Muggianu et al. 1975; K. T. Jacob & K. Fitzner 1977).

Labeling the three mole fractions comprising our mixture of Fe, H_2, and $MgSiO_3$ as x_A, x_B, and x_C, respectively, where $x_A + x_B + x_C = 1$, the ideal free energy of mixing is

$$\Delta\hat{G}_{mix,ideal} = RT(x_A\ln x_A + x_B\ln x_B + x_C\ln x_C). \quad (5)$$

Equation (5) accounts for the ideal entropy of mixing. The excess, or nonideal, free energy of mixing based on the

subregular solution formulation is (J. Ganguly 2001)

$$\begin{aligned}\Delta\hat{G}_{\rm excess} &= x_{\rm A}x_{\rm B}\left(L_{\rm AB}\frac{1}{2}(1+x_{\rm B}-x_{\rm A})+L_{\rm BA}\frac{1}{2}(1+x_{\rm A}-x_{\rm B})\right)\\ &+x_{\rm B}x_{\rm C}\left(L_{\rm BC}\frac{1}{2}(1+x_{\rm C}-x_{\rm B})+L_{\rm CB}\frac{1}{2}(1+x_{\rm B}-x_{\rm C})\right)\\ &\times(1-T/\tau+P/\pi)\\ &+x_{\rm C}x_{\rm A}\left(L_{\rm CA}\frac{1}{2}(1+x_{\rm A}-x_{\rm C})+L_{\rm AC}\frac{1}{2}(1+x_{\rm C}-x_{\rm A})\right)\\ &+x_{\rm A}x_{\rm B}x_{\rm C}L_{\rm ABC},\end{aligned} \tag{6}$$

where L_{ij} are the interaction parameters for species i and j and τ and π parameterize the temperature and pressure dependencies of the nonideal mixing parameters for the $MgSiO_3$–H_2 subregular solution model (L. Stixrude & T. Gilmore 2025). Expressions of the form $\frac{1}{2}(1+x_i-x_j)$ are the normal projections of the mole fractions of the independent component i onto the binary $i-j$ join.

We set $L_{\rm ABC}=0$ in Equation (6) because it is unknown. Indeed, deriving the ternary phase diagram in the absence of explicit values for ternary interaction parameters is the goal of using the Muggianu–Jacob projection method.

4.1. Spinodal

The spinodal curve defines the region where spontaneous decomposition into two phases is required by the negative curvature of the free energy of the mixing surface. It is therefore defined by the condition that the determinant of the Hessian matrix of $\hat{G}_{\rm mix}$ with respect to composition vanishes, i.e.,

$$\det\left(\begin{bmatrix}\frac{\partial^2\hat{G}_{\rm mix}}{\partial x_{\rm A}^2} & \frac{\partial^2\hat{G}_{\rm mix}}{\partial x_{\rm A}\partial x_{\rm B}}\\ \frac{\partial^2\hat{G}_{\rm mix}}{\partial x_{\rm B}\partial x_{\rm A}} & \frac{\partial^2\hat{G}_{\rm mix}}{\partial x_{\rm B}^2}\end{bmatrix}\right)=0. \tag{7}$$

We calculate the derivatives and determinant symbolically on a dense ternary grid ($N=1000$) for each temperature T and pressure P, deriving the spinodal curves for each set of conditions. The resulting spinodal curves delineate the spontaneous phase separation boundaries in the ternary system. Compositions within the spinodals are unstable with respect to spontaneous decomposition into two phases. The binodal, or coexistence curve, lies outside the spinodal, and the region of complete miscibility lies beyond the binodal.

4.2. Binodals

The binodal pairs along the coexistence curves in ternary composition space at specified T and P are defined by applying the criteria for common tangents, satisfying the requirement that $\mu_i^\alpha=\mu_i^\beta$, where μ_i^α is the chemical potential for species i in phase α and μ_i^β is the chemical potential for that same component in phase β. The mixing chemical potentials are related by the first derivative of the free energy of mixing,

$$\mu^\alpha_{i,\rm mix}-\mu^\alpha_{j,\rm mix}=\frac{\partial\hat{G}_{\rm mix}}{\partial x_i^\alpha}, \tag{8}$$

for the independently variable component i and dependent component j in phase α and similarly for phase β.

We found it advantageous to calculate the binodal curves themselves using a convex hull approach (e.g., C. J. Bartel 2022; H. Rossignol et al. 2024; C. P. Dullemond & E. D. Young 2025, in preparation). We calculate the lower facets of a convex hull for the free energy surface in ternary space. The facets are triangles (two-dimensional simplices) that contact the free energy surface. Binodes lie at the facet vertices. The vertices faithfully map the binodal with greater precision than applying Equation (8) directly in cases where the curvature of the free energy surface makes the latter numerically challenging. The approaches agree where the curvatures are numerically robust.

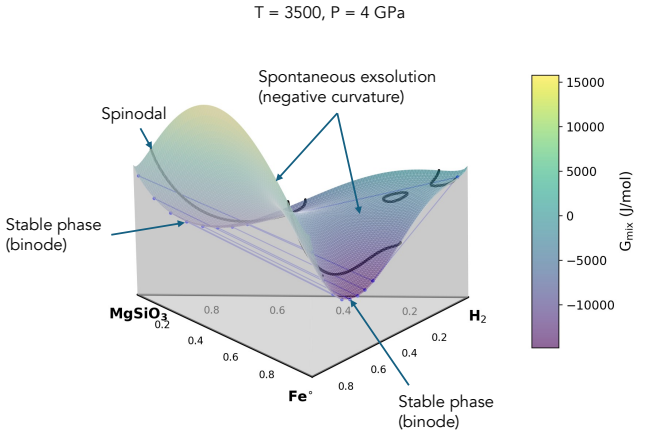

Figure 7. Gibbs free-energy-of-mixing surface, $\hat{G}_{\rm mix}$, in the ternary system $MgSiO_3$–Fe–H_2 for $T=3500$ K and $P=4$ GPa. The heavy black lines show the spinodals denoting the regions of spontaneous decomposition into two phases. Points comprising the binodals are shown in blue connected by tie lines. The blue binodal points define the coexistence curves. Between the binodals and spinodals lies the region of metastability for two phases.

5. Results

5.1. Phase Changes with P and T

Figure 7 shows the resulting Gibbs free energy surface, $\hat{G}_{\rm mix}$, in the ternary system $MgSiO_3$–Fe–H_2 for $T=3500$ K and $P=4$ GPa, where the conditions were chosen for illustration purposes only. The ternary coordinates are the mole fractions of the three components. The heavy black lines show the spinodals. Interior to the spinodals, the curvature of $\hat{G}_{\rm mix}$ is negative, and any infinitesimal perturbation lowers the free energy. Here, phase separation is spontaneous. Each of the coexisting stable phases lies at a point in the phase diagram where the curvature in $\hat{G}_{\rm mix}$ is positive and the points have the same chemical potentials (i.e., equal $\partial\hat{G}_{\rm mix}/\partial x_{\rm i}$). These points, the binodals, are shown as blue points connected by tie lines. They define the coexistence curves for two phases in the phase diagrams. Between the binodals and spinodals lies the region of metastability for two phases.

An example of an isothermal, isobaric phase diagram in ternary space is shown in Figure 8. The diagram is a projection of the free energy surface in the system $MgSiO_3$–Fe–H_2 at

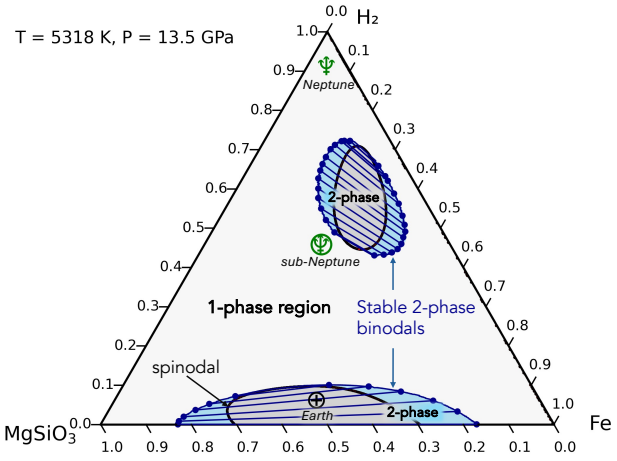

Figure 8. A ternary phase diagram for the system $MgSiO_3$–Fe–H_2 at $T = 5318$ K and $P = 13.5$ GPa. Regions of one-phase stability that lie outside of both the spinodal and binodal curves are shown in pale gray. Regions inside of the spinodals where two liquid phases are ensured are shown in darker gray. The binodals are shown by the blue curves, and coexisting phase compositions for a given bulk composition are shown by the tie lines connecting individual binodes. Regions of two-phase metastability are between the spinodals and binodals and shown in sky blue. Reference planet bulk compositions projected into this ternary space, in mole fractions, are shown for Earth (⊕), our fiducial sub-Neptune (♆), and Neptune (♆), with the weight fractions of H_2 being 0.17%, 2%, and 20%, respectively.

$T = 5318$ K and $P = 13.5$ GPa, where T and P were again chosen for illustration purposes. Ternary coordinates are mole fractions of the three components. Regions of one-phase stability outside of both the spinodal and binodal curves are shown in pale gray. Regions inside of the spinodals are where two liquid phases must occur and are shown in darker gray. The binodals are shown by the blue curves, and the compositions of coexisting two stable phases are shown by the tie lines connecting the binodes. The regions between the spinodals and binodals are where two phases might persist metastably and are shown in sky blue. The ⊕ symbol represents the bulk composition of Earth assuming 0.5 weight percent H_2 in its metal core (E. D. Young et al. 2023). The ♆ symbol represents a fiducial sub-Neptune composition for a bulk H_2 concentration of 2% by mass and the remainder of the planet composed of $MgSiO_3$ silicate and Fe in 2:1 mass proportions. The projected position of Neptune in this space, ♆, is also shown, assuming the bulk H_2 concentration is 20% by weight (approximately 0.9 in mole fraction). Where the hydrogen-rich envelopes do not dominate the mass of H_2, the bulk planet and bulk interior hydrogen concentrations are similar, although not identical.

We constructed a new fiducial model sub-Neptune planet with a total mass of 6 $M_\oplus$ and a bulk H_2 concentration of 2% by mass based on the equations of state for $MgSiO_3$, Fe, and H_2 (see Appendix B for calculation details). In this model, the surface that separates the molten core from the outer H_2-rich envelope is the binodal in the system $MgSiO_3$–H_2. The surface of the supercritical magma ocean is therefore as described by E. D. Young et al. (2024). This surface moves inward as the planet cools, resulting in a lower temperature and higher pressure for the phase boundary; the conditions at the binodal separating the magma ocean from the envelope are tied to the overall thermal state of the planet. Our fiducial model was

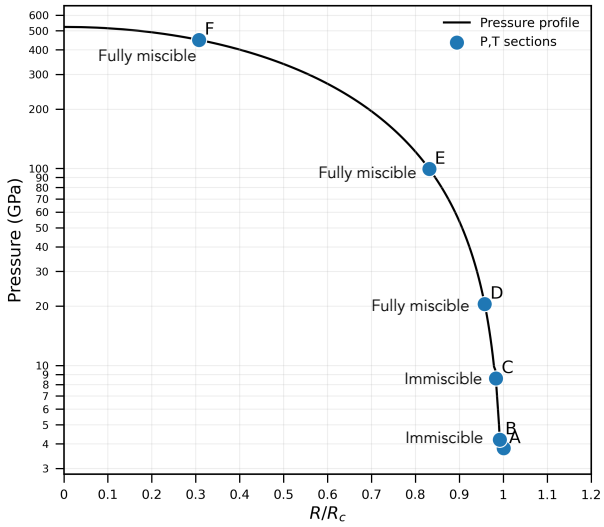

Figure 9. Pressure as a function of radial position along an isentrope in the interior of our fiducial sub-Neptune with a fully miscible core. The envelope–core interface is at $R/R_c = 1$, where R_c is the radius of the interior exclusive of the outer hydrogen-rich envelope (the "core"). The planet total mass is 6 $M_\oplus$ and has a bulk H_2 concentration of 2% by mass. The positions of the isobaric, isothermal phase diagrams in Figure 10 are shown for reference.

chosen to represent an evolved planet with a relatively high pressure of 4 GPa for the binodal.

For these calculations, we prescribe the mass of the planet, the total H_2 abundance, the equilibrium temperature for the atmosphere, and the thermal state of the planet as expressed by the pressure of the binodal defining the outer boundary of the magma ocean, P_S. The pressure of the binodal is a manifestation of the total energy of the planet. Solutions are obtained by iterating between the core and atmosphere structures as follows. As a starting point for the iteration, we assume that all of the H_2 resides in the core and calculate the surface temperature of the magma ocean, i.e., the binodal temperature where one phase becomes unstable relative to two stable phases, melt and envelope, at the prescribed concentration of H_2. This temperature is the reduced temperature for the adiabat in the core (i.e., the surface T_S for given P_S). The shape of the binodal determines the composition of the atmosphere in equilibrium with the melt at T_S and P_S (Figure 2). From the pressure at the base of the atmosphere (the pressure of the binodal) and its composition, we calculate an atmosphere model, including its mass. The lower boundary conditions for the atmosphere are set by the magma-envelope binodal, and the upper boundary is set by the equilibrium temperature. We then subtract the mass of hydrogen in this atmosphere from the core and revise the core calculation, repeating for several iterations until the planet structure converges. The derived P versus radial position for this fiducial sub-Neptune is shown in Figure 9.

Using our ternary Gibbs free energy model, we constructed a sequence of isothermal, isobaric phase diagrams starting near the surface of the magma ocean, where a supercritical magma ocean and a hydrogen-rich envelope coexist, and ending deep in the interior. The results are shown in Figure 10. The location of each of the phase diagrams in our model sub-Neptune is indicated in Figure 9. Focusing on our fiducial sub-Neptune bulk composition, one sees a progression beginning with three phases being in equilibrium at $T = 3500$ K and $P = 3.8$ GPa (Figure 10(A)), a hydrogen-bearing silicate, hydrogen-rich

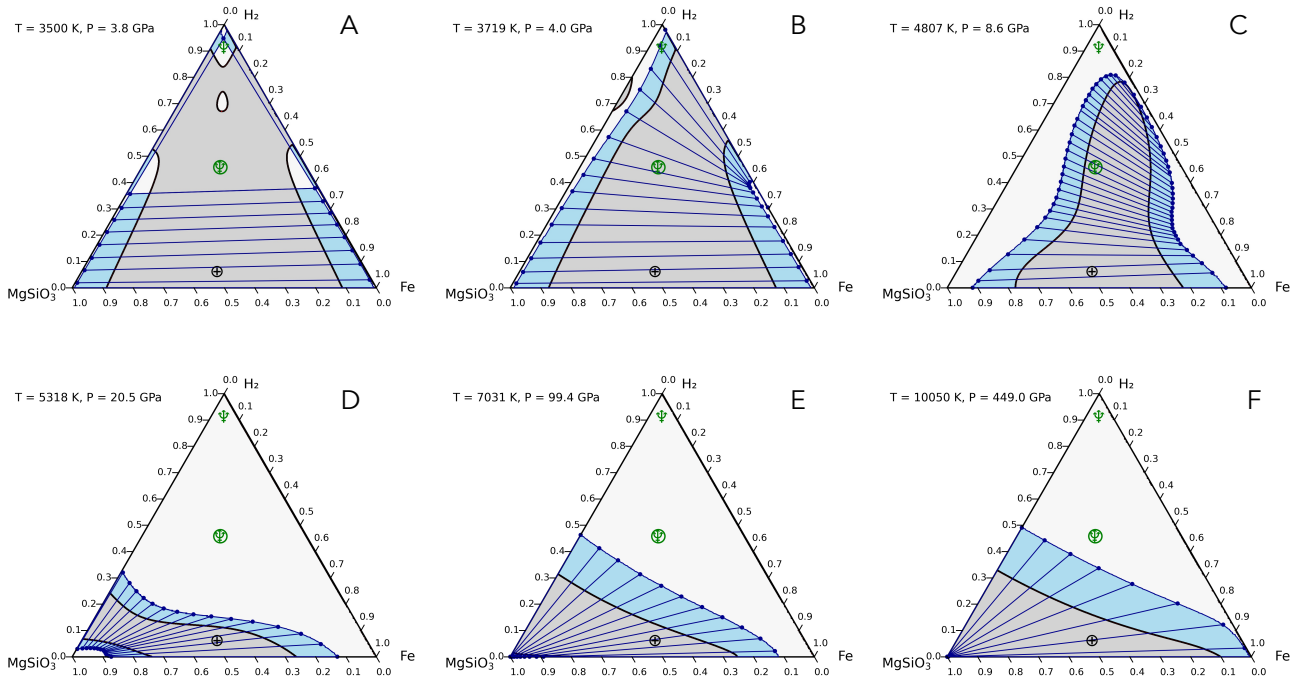

Figure 10. Isothermal, isobaric projections of the Gibbs free-energy-of-mixing surface in the $MgSiO_3$–Fe–H_2 system at six different temperatures and pressures along a nominal T–P path through our fiducial sub-Neptune planet. Concentrations are in mole fractions. The dark gray region is the region of spontaneous exsolution into two phases and is defined by the spinodals (black curves). The blue curves are the binodals defining the coexisting compositions for two stable phases. Example pairs of coexisting compositions are shown by the tie lines between two binodes (blue points) on the binodals. The bulk composition of our reference sub-Neptune with 2 wt% H_2 is shown by the circled Neptune symbol. The bulk composition for Earth, including H in the metal core (E. D. Young et al. 2023), and the bulk composition of Neptune are also shown for reference.

iron metal, and a more hydrogen-rich envelope. As pressure increases deeper through the planet, the phase boundary separating the supercritical magma ocean from the envelope is breached, and our sub-Neptune interior is composed of hydrogen-rich liquid silicate and iron metal (Figure 10(B)). Once pressures exceed about 20 GPa ($T \sim 5000$ K), all compositions with greater than approximately 1% by mass H_2, including the bulk composition corresponding to our fiducial sub-Neptune, are composed of one phase (Figures 10(C) and (D)). The transition at these conditions from two stable phases to one phase is at shallow depths in the planet, at $R/R_c > 0.95$ (Figure 9). Deeper still, the interiors of all planets composed of silicate, iron, and about 1% or greater hydrogen by mass remain as a single phase (Figures 10(E) and (F)). The interiors of sub-Neptunes will have lower mass fractions of hydrogen than the bulk planet values because of the H_2 comprising the envelopes. Our models show that for a bulk of 2% by mass H_2, the interiors of sub-Neptunes similar to our fiducial case are expected to have roughly 1.3% by mass H_2 (Table 1; see discussion below), placing them above the ≈1% threshold separating the two-phase region from the one-phase region at the highest pressures in Figure 10.

This is the main result of these calculations; the interiors of planets with typical proportions of molten rock and iron, when mixed with H_2 at roughly weight percent levels, form a single phase and do not differentiate into a metal core and silicate mantle. Weight percent levels of total hydrogen are expected for sub-Neptunes, as described in the Introduction.

5.2. Sensitivity

It is difficult, if not impossible (e.g., J. J. Gabriel et al. 2020), to quantify the veracity of each of the DFT-MD simulations and experiments that constrain the topology of the $MgSiO_3$–Fe–H_2 ternary phase diagram at the conditions relevant to sub-Neptunes. A quantitative assessment of the accuracy of the isobaric, isothermal phase diagrams is therefore not yet feasible.

We can, however, show changes in phase diagram topologies associated with reasonable variations in the interaction parameters. Arguably, the most uncertain interaction parameter is that for the symmetrical mixing in the $MgSiO_3$–Fe binary, since it has been approximated using the MgO–Fe system. L. Insixiengmay & L. Stixrude (2025) report a fit uncertainty of 5% in this regular interaction parameter, but

Table 1
Sub-Neptune Models for a Planet Mass of 6 $M_\oplus$ and Bulk H_2 Concentration of 2% by Mass

Parameter	Figure 12(A)	Figure 12(B)	Figure 13(A)
$R/R_\oplus$	3.485	2.895	2.618
$R_{core}/R_\oplus$	1.857	1.988	1.827
$M_{core}/M_\oplus$	5.960	5.949	5.962
Metal:silicate core	1:2	0	1:2
Core ρ (g cm^{-3})	5.128	4.175	5.392
T_s	3591	3594	3624
P_s	4	4	4
Bulk planet ρ (g cm^{-3})	0.781	1.363	1.844
Mass fraction envelope	0.655%	0.850%	0.808%
w_{H_2} silicate core	1.33%	1.34%	1.52%
w_{H_2} envelope	100%	77.78%	76.55%

Note. T_s = magma ocean surface temperature (K), P_s = magma ocean surface pressure (GPa), and w_i is the concentration of component i by mass (% where indicated).

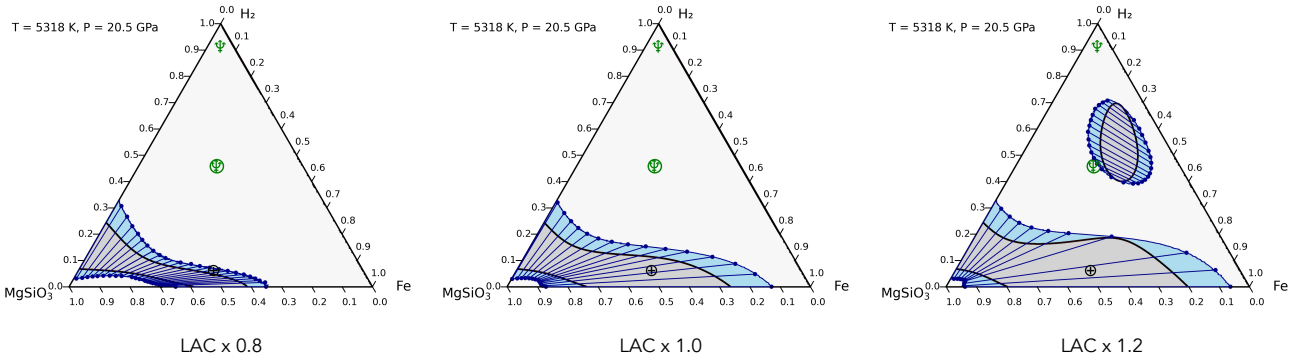

Figure 11. Changes in the topology of the ternary phase diagram shown in Figure 10(D) with variations in the interaction parameter $L_{AC} = L_{CA}$ by +20% and −20%.

this is a measure of precision rather than potential systematic errors. We infer that the actual accuracy is likely lower by a factor of several, as is often the case in practice. Figure 11 shows the changes in topology in the ternary phase diagram shown in Figure 10(D) with ±20% variations in interaction parameter $L_{AC} = L_{CA}$, a spread that is 4 times the fit uncertainty. The changes are relatively minor. The most significant change is that with a greater value for L_{AC}, an island of two-phase stability appears near the composition of our fiducial sub-Neptune. Compositions that fall within this island will be composed of two phases, with their relative proportions given by the lever rule. However, the two phases are much more similar in composition to one another than the silicate mantle and iron. One can see this by comparing the relatively short tie lines in the two-phase island to longer tie lines connecting silicate and metal in the two-phase field occupied by Earth (Figure 11). The appearance and disappearance of this two-phase island is a persistent manifestation of significantly altering the Gibbs free energy surface in these calculations.

Similarly, ∼20% variations in the other interaction parameters (and in many cases much greater variations) have relatively minor effects similar to those shown in Figure 11. Among the parameters comprising the ternary mixing model, the pressure dependence of the mixing in the Fe–H_2 system has the most impact on the results. For separate silicate and Fe-rich metal phases to be stable at depth in our fiducial sub-Neptune with 2% H_2 (e.g., at 100 GPa along the adiabat), the pressure dependence of the interaction parameters in Equation (4) would have to be lower than the adopted value by at least 30%. Stabilization of the two phases results from emergence of the island of two-phase stability in the high-H_2 portion of the phase diagrams (e.g., Figures 8 and 11). However, such a low pressure dependence violates experimental and computational constraints on the relative distributions of H_2 between silicate and Fe metal at the relevant T and P, as described above.

6. Discussion

The complete miscibility of silicate, iron metal, and hydrogen in sub-Neptunes leads to a relatively underdense core as compared with Earth-like layered models. As an illustration, we constructed models that can be used to compare the structures of sub-Neptunes composed of a completely miscible phase in their deep interiors with the more classical "unequilibrated" interiors composed of an inner liquid Fe iron core and an outer liquid silicate mantle. As a predicate, we accept the premise that the interiors of sub-Neptunes should inherit significant mass fractions of hydrogen as a result of the accretion process, and that ingassing of their hydrogen-rich atmospheres after final assembly of the planets may not be the only, or even the primary, mechanism for conveying hydrogen to their interiors. Specifically, we assume that planets form from planetary embryos that accreted hydrogen-rich envelopes that in turn mixed with their molten interiors. The likelihood that primary hydrogen-rich atmospheres intermingled with magma oceans during planet formation has been studied in the context of Earth's formation (H. Mizuno et al. 1980; C. L. Harper & S. B. Jacobsen 1996; E. Jaupart et al. 2017; P. Olson & Z. D. Sharp 2018; E. D. Young et al. 2023) and in the context of sub-Neptune formation and evolution (E. S. Kite et al. 2016, 2019; Y. Chachan & D. J. Stevenson 2018; H. E. Schlichting & E. D. Young 2022). The mass fraction of H_2 that could be accreted from a surrounding protoplanetary disk by a 0.5 $M_\oplus$ embryo is of order 3% (S. Sasaki & K. Nakazawa 1990; E. J. Lee & E. Chiang 2015; S. Ginzburg et al. 2016), with more massive bodies accreting greater mass fractions of hydrogen. The fact that sub-Neptunes do not typically have the maximum mass fractions of H_2 permitted by the accretion process alone speaks to the importance of various loss mechanisms during and after accretion (e.g., J. B. Biersteker & H. E. Schlichting 2019; J. E. Owen et al. 2020).

The model calculations are described in Appendix B, and the results are summarized in Table 1. The fully miscible model is based on the phase diagrams in Figure 10, while the unequilibrated case ignores the phase equilibria. For this comparison, we hold the total mass of the planet constant at 6 $M_\oplus$ for both cases, and we further specify that the total mass fraction of H_2 is 2% for both and that both have the same 1.3% H_2 in their silicate-rich phases (i.e., in their mantles) in order to emphasize the effect of a metal core. In addition, in the case of the completely miscible model, the interface between the outer envelope and the condensed supercritical core is defined by the $MgSiO_3$–H_2 binodal, which we use as an approximation for the ternary phase change as depicted in Figure 10 in panels (A) and (B). In this approximation, the H_2 concentrations in the magma ocean and the outer envelope are controlled by the shape of the binary binodal (e.g., Figure 2). For the envelope, we assume that $MgSiO_3$ speciates to SiO + Mg + O_2 in order to achieve a realistic mean molecular weight for the

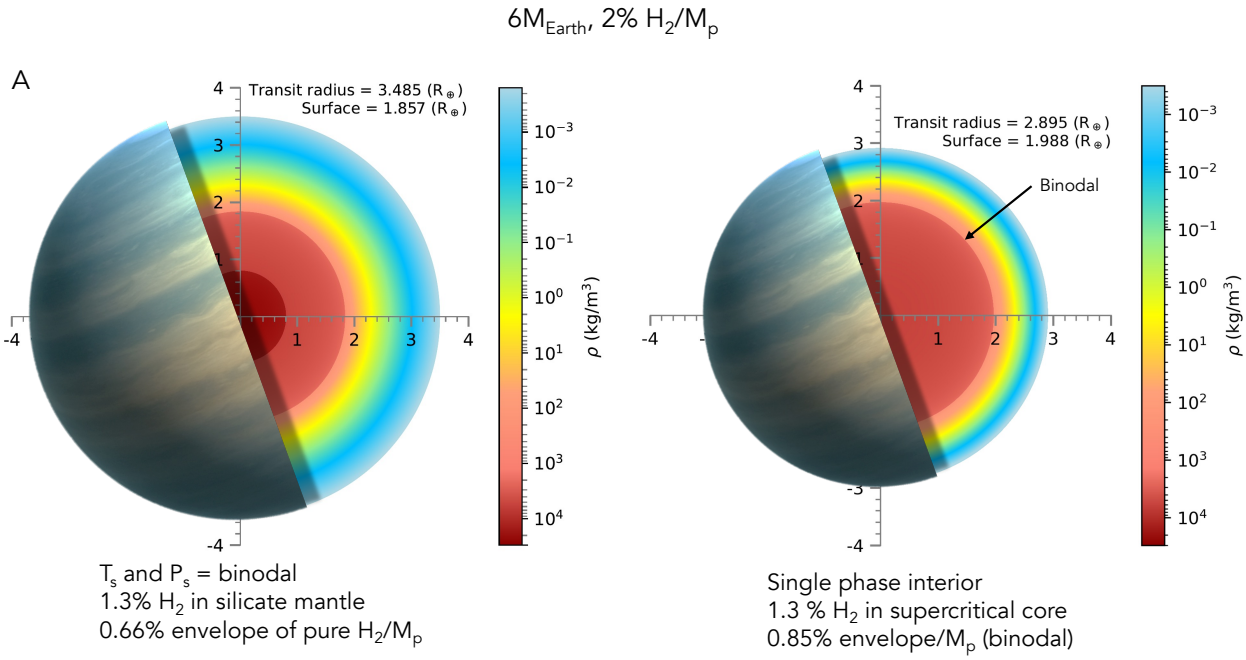

Figure 12. Comparison of two models for a fiducial sub-Neptune. In both cases, the planets have identical masses of 6 $M_\oplus$, equilibrium temperatures of 900 K, and bulk H_2 concentrations of 2% by mass. In panel (A), the planet is an "unequilibrated" structure composed of a pure Fe metallic liquid core overlaid by a $MgSiO_3$ melt with a specified concentration of H_2 to match the fully miscible case in panel (B), in turn overlaid by a pure H_2-rich envelope. The silicate–envelope boundary is specified to be the same T and P as the binodal in panel (B). The planet in panel (B) is composed of a supercritical magma ocean that is a fully miscible ternary mixture of $MgSiO_3$, Fe, and H_2. The surface of the magma ocean is defined by the $MgSiO_3$–H_2 binodal, where $T = 3594$ K and $P = 4.0$ GPa for the melt H_2 concentration of 1.3% by mass. Note that the mass densities are given in kg m^{-3}.

atmosphere (E. D. Young et al. 2024). We further assume that liquid in equilibrium with the gas in the envelope, as prescribed by the binodal as temperature decreases with height in the envelope, rains out immediately, rapidly distilling the envelope phase to pure H_2 higher up. In the case of the "unequilibrated" model, all of the H_2 in the magma ocean phase is in the silicate, with the remaining H_2 comprising the envelope. We specify the temperature and pressure at the magma ocean–envelope interface to be the same as that defined by the binodal in the homogeneous core case for comparison, with values of 3590 K and 4 GPa, respectively.

Figure 12 shows the two different cases for the 6 $M_\oplus$, 2% H_2 sub-Neptune. In the "unequilibrated" case of the core composed of pure Fe metal and a silicate mantle depicted in panel (A), the bulk density of the core is 5.13 g cm^{-3}. The transit radius is 3.49 $R_\oplus$, and the radius of the core is 1.86 $R_\oplus$. The bulk density of the planet is 0.781 g cm^{-3}. In the case of the fully miscible core with an outer boundary defined by the phase change at the binodal, the core has a bulk density of 4.18 g cm^{-3}, considerably less dense than the unequilibrated model. In order to maintain the same imposed total mass of H_2 mandated by our direct comparison, the two models necessarily differ in their respective envelope mass fractions. In the unequilibrated case, the envelope comprises 0.65% of the planet, while in the homogeneous core case, the envelope is 0.85% of the planet. In summary, all else being equal, a planet with an entirely miscible core and an envelope that includes silicates in equilibrium with that core has a smaller radius and a less dense core than its unequilibrated counterpart planet with an envelope of pure H_2, a pure iron core, and H_2 dissolved in the silicate magma.

While useful in illustrating the large range of mass–radius relationships possible for a given total concentration of hydrogen, most studies would consider the assumption of a pure H_2 envelope inadequate (e.g., H. Chen & L. A. Rogers 2016; E. S. Kite et al. 2019; J. L. Bean et al. 2021; H. E. Schlichting & E. D. Young 2022; A. Werlen et al. 2025). More importantly for our purpose, the comparison above does not isolate the effect of differentiation of metal and silicate, as evident from a simple analysis of the result.

The ratio of the core radius for the unequilibrated model in Figure 12(A) to that in Figure 12(B) is 0.93, while the ratio of their transit radii is 1.19. The mismatch is due to their different envelopes and can be understood as follows. Since the planets have the same upper atmosphere temperatures and molecular weights, the transit radii in this case depend largely on the radial thicknesses of the convective layers of the envelopes as well as on the cores. We can understand these influences on the radii of the planets in the two models using an approximation for the radial temperature gradient due to convection for an ideal gas (taken to be the limiting case of the isentrope),

$$\nabla T = -\frac{(\gamma - 1)}{\gamma}\frac{\mu_{\rm mol}}{k_{\rm B}}g, \tag{9}$$

where $\mu_{\rm mol}$ is the mean molecular weight of the gas, γ is the heat capacity ratio, $k_{\rm B}$ is the Boltzmann constant, and g is the acceleration of gravity. The decrease in temperature from the surface to the radiative–convective boundary comprising the outer radius of the convective layer of the envelope is about the same in the models in Figures 12(A) and (B), basically $T_{\rm s}$–$T_{\rm eq}$. With the approximation of equal dT values and equal heat capacity ratios, the ratio of radial thicknesses of the atmospheres, $\Delta R = R_{\rm p} - R_{\rm core}$, for the models in

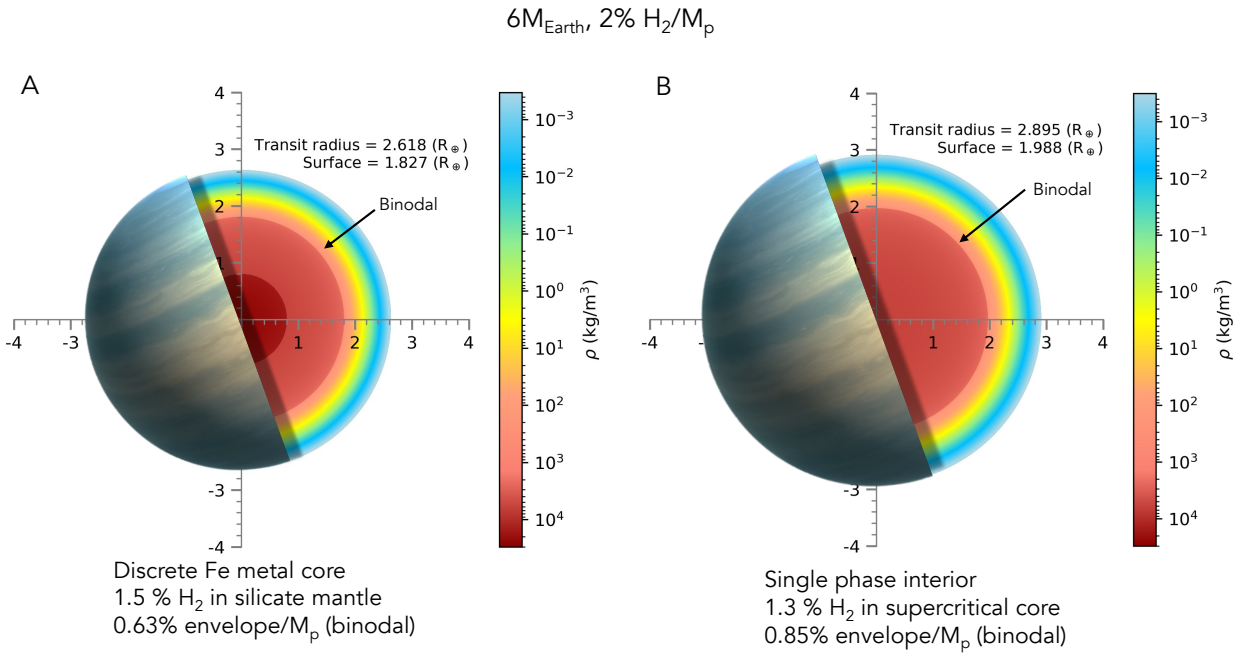

Figure 13. Comparison of two models for a fiducial sub-Neptune. In both cases, the planets have identical masses of 6 $M_\oplus$, equilibrium temperatures of 900 K, and bulk H_2 concentrations of 2% by mass. In panel (A), the planet is composed of a pure Fe metallic liquid core overlaid by a supercritical mixture of $MgSiO_3$ and H_2, which is in turn overlaid by a H_2-rich envelope. The silicate–envelope boundary is the binodal (solvus) at a pressure of 4 GPa. The planet in panel (B) is the same as in Figure 12(B) and is a fully miscible ternary mixture of $MgSiO_3$, Fe, and H_2.

Figures 12(A) and (B) is

$$\frac{\Delta R_A}{\Delta R_B} \sim \frac{\mu_{mol,B}}{\mu_{mol,A}} \frac{(R_{core}\,\rho_{core})_B}{(R_{core}\,\rho_{core})_A}, \tag{10}$$

where ΔR_A and ΔR_B are the thicknesses of the envelopes for the models in panels (A) and (B) in Figure 12. The first term on the right-hand side of Equation (10) is the ratio of molecular weights. The mean molecular weight of the envelope for the unequilibrated pure H_2 envelope is, by design, 2.3 amu (e.g., H_2 with an assumed He concentration) throughout, while the mean molecular weight of the envelope in the single-phase, fully miscible interior model is 3.5 amu near the base, where much of the mass resides, transitioning upward to 2.3 amu at lower densities. The first term can thus be approximated as $3.5/2.3 = 1.52$. The second term can be evaluated using the radius and density data for the cores in Table 1, yielding a value of 0.871. The simplified prediction for the ratio $(R_p - R_{core})_A/(R_p - R_{core})_B$ from Equation (10) is 1.33. The full model ratio is 1.79 (Table 1), the difference being attributable to the effects of convective inhibition, a moist adiabat, and other factors not included in this simple analysis. These calculations illustrate that the greater density of the core in the unequilibrated case compared with the fully miscible core should decrease the radius of the planet, all else being equal, but the difference in mean molecular weights in the lower atmospheres overwhelms this effect.

In order to better isolate the effect of the core density on the bulk density of our fiducial 6 $M_\oplus$ planet, we compare the fully miscible interior model in Figure 12(B) with a similar model in which the only difference is that there is a pure Fe, Earth-like metal core. The Fe metal and silicate are in 1:2 proportions. Again, the total planet mass and mass fraction of hydrogen are maintained. The result is shown in Figure 13. Here the effects on bulk density due to the characteristics of the differentiated core and the fully miscible core are evident. The presence of a pure Fe core interior to the silicate increases the overall core density of the planet from 4.18 to 5.39 g cm^{-3}. The planet with the pure Fe central core has a smaller transit radius by about 10% compared with the fully miscible model, with values of 2.62 $R_\oplus$ and 2.90 $R_\oplus$ for the two bodies, respectively. The pure Fe central core case results in a greater bulk density for the planet of 1.84 g cm^{-3} compared with the fully miscible case where the bulk density is 1.36 g cm^{-3}, an increase of 35%.

Although the difference in transit radii is impacted by core densities, here again the envelopes also contribute. However, the important conclusion is that the envelopes enhance the effects of different core densities on the average planet density in this case, rather than opposing the effects of core densities as in the previous case (Table 1).

The result of this comparison of models in Figure 13 is that substituting a single, supercritical silicate–Fe–H_2 phase for an Earth-like central Fe metal core and an overlying H-bearing silicate magma ocean affects the observable bulk density of the planet when the total mass fraction of H_2 for the planet is the same, with a difference in radius of order 10%. An even more significant change is the differences in the central core temperatures. The central temperature of the Fe-core case is about double that of the fully miscible case. The sum of thermal and gravitational potential energies for the two planets is therefore also different, by about 30%, with values of -3.872×10^{33} and -4.995×10^{33} J for the fully miscible and Fe-core cases, respectively. While they are of the same mass and the same total H_2 mass fraction, these planets would have arrived at their respective configurations along very different evolutionary paths.

7. Conclusions

We show that based on our present understanding of the phase equilibria of the $MgSiO_3$–Fe–H_2 system, the interiors of sub-Neptunes are unlikely to be composed of a discrete silicate mantle and iron core during, and presumably after, their magma ocean phase of evolution. Discrete silicate and metal phases are expected to occur in only the very shallowest depths of these planets. The mixed-phase core is underdense, with a compressed bulk density closer to 4.2 g cm^{-3} for a core mass of 6 $M_\oplus$ as compared with the Earth-like compressed bulk densities of 5.4 g cm^{-3} that apply for analogous planets with discrete metal cores. The boundary between this fully miscible core and the outer H_2-rich envelopes corresponds to the phase change from a supercritical melt to a coexisting melt and envelope. The base of the envelope is predicted to have significant fractions of heavy elements.

These results are important for motivating investigations into the equations of state for these core materials, as well as the chemistry of sub-Neptune cores. With our current assumptions of linear mixing of densities among the three components and compressibilities similar to $MgSiO_3$, the effect of the supercritical, one-phase cores on the bulk density of the planets is on the order of 30%. We have shown that miscibility is a mechanism for storing hydrogen throughout the cores of these planets that is distinct from extrapolations of solubilities of gases into silicate melt. The physical chemistry is much richer and deserving of further exploration if we are to understand this important class of planets. With this in mind, it is tempting to extrapolate these results to the more massive Neptune-like planets as well; might ice giants contain within them supercritical mixtures dominated by Mg, Si, O, Fe, and H? We are not aware of any data or strong arguments against such a proposition.

Acknowledgments

We acknowledge financial support from NASA grant 80NSSC24K0544 (Emerging Worlds program). Suggestions by three anonymous reviewers are gratefully acknowledged.

Appendix A
DFT Simulations

We use DFT-MD to validate mixing along the binary joins involving silicate. DFT is based on the concept that the Schrödinger equation may be reformulated so that the charge density, rather than the total wave function, is the central quantity (P. Hohenberg & W. Kohn 1964; W. Kohn & L. J. Sham 1965). We follow the methods described by A. Gupta et al. (2025), L. Insixiengmay & L. Stixrude (2025), and L. Stixrude & T. Gilmore (2025). Briefly, we use DFT to determine the ground-state electron densities and energy states of the systems. The Kohn–Sham potentials and orbitals (wave functions) are represented with a complete orthogonal set of basis functions using the projector augmented wave method, as implemented in the VASP code (G. Kresse & J. Furthmöller 1996; G. Kresse & D. Joubert 1999).

Simulations are performed in the canonical ensemble in which the total number of particles, the volume, and the temperature are held fixed (S. Nosé 1984; W. G. Hoover 1985). At each time step, the atomic coordinates, momenta, and forces are recorded, as are the internal energy and stress tensor computed via DFT.

The methods for the two-phase simulations are as described by A. Gupta et al. (2025), L. Insixiengmay & L. Stixrude (2025) and L. Stixrude & T. Gilmore (2025). The simulations are initiated in the following manner. We first perform one-phase simulations on each of the two pure phases. The volumes of the periodic simulation cell are identical in the two phases, and the number densities are chosen so that the equilibrated pressure is identical in the two phases. We then initiate a two-phase simulation by constructing a supercell, consisting of half one phase and half the other. We then allow the atoms to move in accordance with the DFT forces acting on them. Mass exchange occurs spontaneously according to the chemical driving forces manifested in the DFT forces acting on the atoms.

For the $MgSiO_3$–H_2 system, solid $MgSiO_3$ comprising 200 atoms was run for 5 ps at 6000 K in order to ensure that the solid structure melted. It was then cooled to the initial temperatures for the simulations and allowed to equilibrate for an additional 3–5 ps. The same equilibration was performed for the pure H_2 phase, consisting of 176 atoms, prior to joining the two phases as shown in Figure 3.

Over the course of the simulations, the two-phase system evolved to establish a dynamic equilibrium such that the composition of the two phases was no longer changing with time. The higher-temperature 4000 K simulation ran for 13.5 ps, and the lower-temperature 3000 K simulation ran for 16.5 ps. The composition of each phase was monitored by tracking the concentration of each atom type in each phase.

By the end of the simulations, the 4000 K system evolved into a single phase. The weight percent of H across the entire simulation reached 4.3%, which is the weight percent of H in the entire system. The 3000 K simulation remained immiscible for the duration of the simulation. The weight percent of H in the silicate-rich phase never exceeded 1%, while it remained the dominant species in the H-rich phase.

The methods for the $MgSiO_3$–Fe system were essentially the same, where both phases were heated to melting, then equilibrated in P and T prior to the initiation of mixing. The model consists of 18 Mg atoms, 18 Si atoms, 54 O atoms, and 76 Fe atoms. We checked the convergence of the results in Figure 5 by decreasing the time steps, settling on steps of 0.5 fs. Fe atoms are non-spin-polarized in these calculations. Band gaps are therefore not properly modeled, but we do not anticipate that this simplification changes the basic result of miscibility. See L. Insixiengmay & L. Stixrude (2025) for an assessment of the effects of spin polarization on miscibility in the MgO–Fe system. Future models should include spin polarization.

Appendix B
Planet Models

Core structure. To derive the core structure, we solve the following system of equations (e.g., S. Seager et al. 2007):

$$\frac{dm}{dr} = 4\pi r^2 \rho, \tag{11}$$

$$\frac{dP}{dr} = -\frac{Gm\rho}{r^2}, \tag{12}$$

and

$$\left(\frac{dT}{dr}\right)_S = -\gamma(\eta)\frac{T}{P}\rho g, \tag{13}$$

where m is the mass contained within a radius r, ρ is the mass density, and $\gamma(\eta)$ is the Grüneisen parameter that varies with P and T through the compressibility factor $\eta = \rho/\rho_0$. Here we have assumed that the core is fully convective, with a limiting isentropic dT/dP gradient. Numerically integrating Equations (11)–(13) for the core and mantle yields a density and temperature profile for the core.

Material properties of the core. For liquid silicate densities, we use an equation-of-state fit to the $MgSiO_3$ liquid properties determined by N. de Koker & L. Stixrude (2009) using the algorithms of A. S. Wolf & D. J. Bower (2018). Total pressure is computed by combining the elastic (cold) compression term from a Vinet equation of state with thermal pressure contributions, following the formulation of A. S. Wolf & D. J. Bower (2018). The thermal pressure corrections consist of vibrational energy contributions (ΔP_E) and deviations along the isentrope (ΔP_S). These corrections are calculated self-consistently as functions of the compressibility factor $\eta = \rho/\rho_0$, temperature T, and volume V. The effective heat capacity C_P also varies with the compressibility factor η along the adiabat.

For liquid iron, we use a Vinet equation of state modified to include thermal pressure from Y. Kuwayama et al. (2020). The Grüneisen parameter is a simple function of the compression ratio, which in turn determines the thermal contribution to pressure.

Mixing. For regions of the planet inside the binodal, hydrogen, Fe, and $MgSiO_3$ melt are completely miscible and form a homogeneous mixture. We assume that the equation of state for the mixture of $MgSiO_3$ and H_2 is the same as that for $MgSiO_3$, with an adjustment for the effect of H_2 on the density, as described below. We include the effects of Fe by mixing compressed Fe and the $MgSiO_3$–H_2 mixture linearly, also described below.

The presence of hydrogen in the silicate melt reduces its density. Our DFT-MD simulations show that at 6000 K and 3.5 GPa, the density of the mixed phase decreases from 2.5 g cm^{-3} for pure $MgSiO_3$ to 1.35 g cm^{-3} for the mixture of $MgSiO_3$ and 4% H_2. We find that a linear mixture of the compressed densities of $MgSiO_3$ and H_2 by volume reproduces this shift in density at these conditions. We include the effects of H_2 on the density of the supercritical melt by calculating the density of the mixture at the pressures and temperatures of the surface of the magma ocean, ρ_0, as these conditions resemble those for the simulations. The density of the mixture is obtained using

$$\frac{1}{\hat{V}_{\rm mix}} = x_{\rm H_2}\frac{1}{\hat{v}_{\rm H_2}} + x_{\rm sil}\frac{1}{\hat{v}_{\rm sil}}, \tag{14}$$

where $\hat{v}_{\rm H_2}$ and $\hat{v}_{\rm sil}$ are the molar volumes and $x_{\rm H_2}$ and $x_{\rm sil}$ are the mole fractions of hydrogen and silicate in the binary mixture. Densities are then $MW_{\rm mix}/\hat{V}{\rm mix}$, where $MW_{\rm mix}$ is the molecular weight of the mixture. Molar volumes are obtained from densities and the equations of state using ρ_i/MW_i. This formulation is consistent with the assumption that the addition of H does not greatly affect the equation of state. We fixed the densities to be 0.09 and 2.5 g cm^{-3} for H_2 and silicate, respectively, at the surface of the magma ocean. These values come from the equations of state for hydrogen from G. Chabrier et al. (2019) and our ab initio molecular dynamics simulations of $MgSiO_3$ melt at 6000 K and 3.5 GPa.

We model Fe dissolved in a supercritical silicate–H_2 melt by assigning Fe a partial molar volume that reflects Fe occupation of Mg-like cation sites within the silicate melt framework. We let $\phi \in [0, 1]$ denote the fraction of the pure $MgSiO_3$ formula-unit molar volume attributable to the Mg site, and let $\alpha = (r_{\rm Fe}/r_{\rm Mg})^3$ scale these site volumes by the ratio of octahedrally coordinated ionic radii (R. D. Shannon 1976). If $\bar{V}^{\rm pure}_{\rm MgSiO_3} = MW_{\rm MgSiO_3}/\rho^{\rm pure}_{\rm MgSiO_3}$ is the molar volume of pure $MgSiO_3$ at the local P and T, the Fe-site partial molar volume is

$$\bar{V}^{\rm eff}_{\rm Fe\ site} = \phi\ \alpha\ \bar{V}^{\rm pure}_{\rm MgSiO_3}(P, T), \tag{15}$$

and the corresponding effective partial Fe density is

$$\rho^{\rm eff}_{\rm Fe\ site} = \frac{MW_{\rm Fe}}{\bar{V}^{\rm eff}_{\rm Fe\ site}}. \tag{16}$$

Assuming additivity of specific volumes (no excess mixing volume), the density of the miscible melt with Fe mass fraction $w_{\rm Fe}$ is given by the harmonic mean

$$\frac{1}{\rho_{\rm mix}} = \frac{1 - w_{\rm Fe}}{\rho_{\rm MgSiO_3+H_2}} + \frac{w_{\rm Fe}}{\rho^{\rm eff}_{\rm Fe}}, \tag{17}$$

where $\rho_{\rm MgSiO_3+H_2}$ is the density of the $MgSiO_3 + H_2$ mixture derived at P and T. An empirical value for ϕ of 0.5 is obtained from the MgO–Fe system (L. Insixiengmay & L. Stixrude 2025). We use the MgO–Fe rather than the $MgSiO_3$–Fe simulations because in the former case, fixed number of atoms, pressure, temperature ensemble simulations were used to derive volumes at constant pressure, affording the required volumetric data for mixing. In the models reported here, we use $r_{\rm Fe} = 0.078$ nm (VI, high spin) and $r_{\rm Mg} = 0.072$ nm. The results are insensitive to the precise values for these constants.

Structure of the envelope. The structure of the envelope is obtained using a model similar to that published previously by E. D. Young et al. (2024). We numerically integrate the equations,

$$\frac{dm_{\rm Atm}}{dr} = 4\pi r^2\rho, \tag{18}$$

$$\frac{dP}{dr} = -\frac{Gm\rho}{r^2}, \tag{19}$$

and

$$\frac{dT}{dr} = \min\left(\nabla T|_{\rm rad}, \nabla T|_{\rm conv}\right), \tag{20}$$

where $m_{\rm Atm}$ is the mass of the atmosphere, m is the total mass contained within a radius r, and the numerical integration is from the magma ocean outward. For the envelope equation of state (densities at P and T), we use the tabulated function from G. Chabrier et al. (2019).

The envelope is divided into three regions. The bulk of the lower region is convective. Because the vapor and silicate melt are in equilibrium, we use the moist pseudoadiabat of R. J. Graham et al. (2021) to evaluate the convective temperature gradient $\nabla T_{\rm conv}$. The molar heat capacities

required to evaluate the pseudoadiabat from R. J. Graham et al. (2021) are obtained from the NIST thermodynamic database (M. Chase 1998), where we assume that the vapor silicate component speciates to SiO, Mg, and O_2. If we scale the pseudoadiabat by the adiabatic temperature gradient implied by the H_2 equation of state, our results presented here are virtually identical if the binodal pressure is taken to be 2 GPa instead of 4 GPa. This lower pressure for the binodal would imply a younger, less evolved planet.

Hindrance of convection due to the mass load of heavy elements at relatively high temperatures must be included, as described previously for similar circumstances by W. Misener et al. (2023). By including the Ledoux criterion rather than just the Schwarzschild criterion for convection, the calculations permit development of a radiative layer at the base of the atmosphere that transports the intrinsic heat coming from the magma ocean upward (T. Guillot 2010; W. Misener et al. 2023). The intrinsic luminosity due to the heat emanating from the core to space becomes a determining factor for the structure of the atmosphere. Since radiative diffusion relies on the local luminosity, the temperature gradient due to radiative diffusion includes the radially dependent luminosity, $L(r)$. At depths well below the radiative–convective boundary, stellar radiation cannot penetrate the atmosphere. Therefore, at these depths, the radiative diffusion is given by

$$\nabla T_{\rm rad} = -\frac{3\kappa\rho L(r)}{64\pi\sigma T^3 r^2}, \tag{21}$$

where $L(r)$ is taken to be the intrinsic luminosity, $L_{\rm int}$. The intrinsic luminosity is manifested by the radiation temperature at the top of the magma ocean, $L_{\rm int} = \sigma(T_{\rm int})^4 4\pi R_s^2$. The intrinsic temperature $T_{\rm int}$ is defined by the net upward component of the flux corresponding to the surface temperature of the magma ocean as prescribed by the local opacity. The surface temperature and optical depth at the surface therefore define $T_{\rm int}$ according to (e.g., K. Heng et al. 2014)

$$T_{\rm int} = T_s\left(\frac{4}{3(\tau_s + 1)}\right)^{1/4}, \tag{22}$$

where using 1 instead of 3/4 in the denominator term is an approximation for a spherical geometry and the subscript s refers to properties at the surface of the magma ocean. The optical depth at the location is obtained using the metallicity prescribed by the mixing ratios of SiO and Mg in the envelope as prescribed by the coexistence binodal curve at those conditions.

We use the criterion for convective inhibition given by S. Markham et al. (2022), expressed in terms of the mole fraction of heavy elements relative to H_2, $1 - xH_2$,

$$(1 - xH_2)_{\rm critical} = 1/((\Delta\hat{H}_c/(RT) - 1)(\epsilon - 1)), \tag{23}$$

where $\Delta\hat{H}_c$ is the latent heat of condensation per mole of condensate and ϵ is the ratio of the mean molecular weight of the condensable gas to H_2, where we assume that $MgSiO_3$ in the gas phase instantly speciates to SiO, Mg, and O_2. The heat of condensation is calculated as $\Delta\hat{H}_c = \hat{H}_{MgSiO_3} - \hat{H}_{SiO} - \hat{H}_{Mg} - \hat{H}_{O_2}$, where the poorly known effect of H dissolved in the condensate on the latent heat is assumed to be of minor importance. Molar enthalpies as a function of temperature are obtained from the NIST thermodynamic database (M. Chase 1998). Where the mole fraction of heavy elements exceeds $(1 - xH_2)_{\rm critical}$, the temperature gradient is given by Equation (21).

The radiative transfer attending the transition from the convective layer to the upper radiative layer in the atmosphere is approximated using Eddington's two-stream 1D solution for temperature,

$$T(r)^4 = \frac{3}{4}T_{\rm int}^4(1 + \tau(r)) + \frac{3}{4}T_{\rm eq}^4\left(1 - \frac{1}{2}e^{-\tau(r)}\right), \tag{24}$$

where both the intrinsic heat transported from below and the stellar radiation are accounted for in one dimension. We implement the transition from convection to radiation where the gradient in T is due to radiation, given by

$$\frac{dT}{d\tau(r)} = \frac{1}{4T(r)^3}\left(\frac{3}{4}T_{\rm int}^4 + \frac{3}{8}T_{\rm eq}^4 e^{-\tau(r)}\right),$$

and

$$\nabla T_{\rm rad} = \frac{dT}{d\tau(r)}\frac{d\tau(r)}{dr} \tag{25}$$

becomes less than $\nabla T_{\rm conv}$. The two-stream solution blends radiative diffusion where optical depths are sufficient to sustain diffusion smoothly to the optically thin upper atmosphere where there is free radiation.

We define the radius of the planet using the chord optical depth as formulated by T. Guillot (2010) coupled with the opacities from R. S. Freedman et al. (2014) with metallicities corresponding to the composition of the gas (essentially pure H_2 at relevant heights for the outer atmosphere).

ORCID iDs

Edward D. Young https://orcid.org/0000-0002-1299-0801
Aaron Werlen https://orcid.org/0009-0005-1133-7586
Sarah P. Marcum https://orcid.org/0009-0001-6858-9849
Lars Stixrude https://orcid.org/0000-0003-3778-2432
Cornelis P. Dullemond https://orcid.org/0000-0002-7078-5910

References

Adibekyan, V., Dorn, C., Sousa, S. G., et al. 2021, Sci, 374, 330
Ahrer, E.-M., Radica, M., Piaulet-Ghorayeb, C., et al. 2025, ApJL, 985, L10
Badro, J., Aubert, J., Hirose, K., et al. 2018, GeoRL, 45, 240
Bartel, C. J. 2022, JMatS, 57, 10475
Bean, J. L., Raymond, S. N., & Owen, J. E. 2021, JGRE, 126, e2020JE006639
Benneke, B., Roy, P.-A., Coulombe, L.-P., et al. 2024, arXiv:2403.03325
Benneke, B., Wong, I., Piaulet, C., et al. 2019, ApJL, 887, L14
Biersteker, J. B., & Schlichting, H. E. 2019, MNRAS, 485, 4454
Bitsch, B., Raymond, S. N., & Izidoro, A. 2019, A&A, 624, A109
Chabrier, G., Mazevet, S., & Soubiran, F. 2019, ApJ, 872, 51
Chachan, Y., & Stevenson, D. J. 2018, ApJ, 854, 21
Chase, M. 1998, NIST-JANAF Thermochemical Tables (4th ed.; Melville, NY: AIP)
Chen, H., & Rogers, L. A. 2016, ApJ, 831, 180
Davenport, B., Kempton, E. M.-R., Nixon, M. C., et al. 2025, ApJL, 984, L44
de Koker, N., & Stixrude, L. 2009, GeoJI, 178, 162
Doyle, A. E., Young, E. D., Klein, B., Zuckerman, B., & Schlichting, H. E. 2019, Sci, 366, 356
Felix, L., Kitzmann, D., Demory, B.-O., & Mordasini, C. 2025, A&A, 701, A296
Fortney, J. J., Marley, M. S., & Barnes, J. W. 2007, ApJ, 659, 1661
Freedman, R. S., Lustig-Yaeger, J., Fortney, J. J., et al. 2014, ApJS, 214, 25
Fressin, F., Torres, G., Charbonneau, D., et al. 2013, ApJ, 766, 81

Fukai, Y. 1992, in Some Properties of the Fe-H System at High Pressures and Temperatures, and their Implications for the Earth's Core, ed. Y. Syono & M. H. Manghnani (Washington, DC: AGU), 373
Fulton, B. J., Petigura, E. A., Howard, A. W., et al. 2017, AJ, 154, 109
Gabriel, J. J., Paulson, N. H., Duong, T. C., et al. 2020, JOM, 73, 149
Ganguly, J. 2001, in Solid Solutions in Silicate and Oxide Systems, ed. C. A. Geiger (Middlesex: Mineralogical Society of Great Britain and Ireland), 37
Ginzburg, S., Schlichting, H. E., & Sari, R. 2016, ApJ, 825, 29
Graham, R. J., Lichtenberg, T., Boukrouche, R., & Pierrehumbert, R. T. 2021, PSJ, 2, 207
Guillot, T. 2010, A&A, 520, A27
Gupta, A., & Schlichting, H. E. 2019, MNRAS, 487, 24
Gupta, A., Stixrude, L., & Schlichting, H. E. 2025, ApJL, 982, L35
Harper, C. L., & Jacobsen, S. B. 1996, Sci, 273, 1814
Heng, K., Mendonca, J. M., & Lee, J.-M. 2014, ApJS, 215, 4
Hohenberg, P., & Kohn, W. 1964, PhRv, 136, B864
Hoover, W. G. 1985, PhRvA, 31, 1695
Insixiengmay, L., & Stixrude, L. 2025, E&PSL, 654, 119242
Jacob, K. T., & Fitzner, K. 1977, TcAc, 18, 197
Jaupart, E., Charnoz, S., & Moreira, M. 2017, Icar, 293, 199
Jiang, G., Li, Y.-x., & Liu, Y. 2011, TNMSC, 21, 1130
Jura, M., & Young, E. 2014, AREPS, 42, 45
Kite, E. S., Fegley, Bruce, J., Schaefer, L., & Ford, E. B. 2019, ApJ, 887, L33
Kite, E. S., Fegley, B., Jr., Schaefer, L., & Gaidos, E. 2016, ApJ, 828, 80
Kohn, W., & Sham, L. J. 1965, PhRv, 140, A1133
Kresse, G., & Furthmöller, J. 1996, ComMS, 6, 15
Kresse, G., & Joubert, D. 1999, PhRvB, 59, 1758
Kuwayama, Y., Morard, G., Nakajima, Y., et al. 2020, PhRvL, 124, 165701
Lee, E. J., & Chiang, E. 2015, ApJ, 811, 41
Lee, S. K., & Kim, S. J. 2001, Calphad, 25, 97
Lichtenberg, T. 2021, ApJ, 914, L4
Madhusudhan, N., Nixon, M. C., Welbanks, L., Piette, A. A. A., & Booth, R. A. 2020, ApJL, 891, L7
Manser, C. J., Gänsicke, B. T., Eggl, S., et al. 2019, Sci, 364, 66
Markham, S., Guillot, T., & Stevenson, D. 2022, A&A, 665, A12
Misener, W., Schlichting, H. E., & Young, E. D. 2023, MNRAS, 524, 981
Mizuno, H., Nakazawa, K., & Hayashi, C. 1980, E&PSL, 50, 202
Muggianu, Y., Gambino, M., & Bros, J. 1975, JChTh, 7, 1051
Nosé, S. 1984, MolPh, 52, 255
Olson, P., & Sharp, Z. D. 2018, E&PSL, 498, 418
Owen, J. E., Shaikhislamov, I. F., Lammer, H., Fossati, L., & Khodachenko, M. L. 2020, SSRv, 216, 129
Owen, J. E., & Wu, Y. 2013, ApJ, 775, 105
Payne-Gaposchkin, C. H. 1925, PhD thesis, Radcliffe College
Rogers, J. G., Dorn, C., Aditya Raj, V., Schlichting, H. E., & Young, E. D. 2025, ApJ, 979, 79
Rogers, J. G., Owen, J. E., & Schlichting, H. E. 2024, MNRAS, 529, 2716
Rossignol, H., Minotakis, M., Cobelli, M., & Sanvito, S. 2024, J. Chem. Inf. Model., 64, 1828
San-Martin, A., & Manchester, F. 1990, Bulletin of Alloy Phase Diagrams, 11, 173
Sasaki, S., & Nakazawa, K. 1990, Icar, 85, 21
Schlichting, H. E., & Young, E. D. 2022, PSJ, 3, 127
Seager, S., Kuchner, M., Hier-Majumder, C. A., & Militzer, B. 2007, ApJ, 669, 1279
Shakya, A., Ghosh, D. B., Jackson, C., Morra, G., & Karki, B. B. 2024, NatSR, 14, 18739
Shannon, R. D. 1976, AcCrA, 32, 751
Shorttle, O., Jordan, S., Nicholls, H., Lichtenberg, T., & Bower, D. J. 2024, ApJL, 962, L8
Stixrude, L., & Gilmore, T. 2025, Research Square, doi:10.21203/rs.3.rs-6630955/v1
Stixrude, L., & Karki, B. 2005, Sci, 310, 297
Tagawa, S., Sakamoto, N., Hirose, K., et al. 2021, NatCo, 12, 2588
Trierweiler, I. L., Doyle, A. E., Melis, C., Walsh, K. J., & Young, E. D. 2022, ApJ, 936, 30
Trierweiler, I. L., Doyle, A. E., & Young, E. D. 2023, PSJ, 4, 136
Vazan, A., Ormel, C. W., Noack, L., & Dominik, C. 2018, ApJ, 869, 163
Wahl, S. M., & Militzer, B. 2015, E&PSL, 410, 25
Werlen, A., Dorn, C., Schlichting, H. E., Grimm, S. L., & Young, E. D. 2025, ApJL, 988, L55
Wohl, K. 1946, Trans. Am. Inst. Chem. Eng., 42, 215
Wohl, K. 1953, Chemical Engineering Progress, 49, 218
Wolf, A. S., & Bower, D. J. 2018, PEPI, 278, 59
Young, E. D., Shahar, A., & Schlichting, H. E. 2023, Natur, 616, 306
Young, E. D., Stixrude, L., Rogers, J. G., Schlichting, H. E., & Marcum, S. P. 2024, PSJ, 5, 268
Yuan, L., & Steinle-Neumann, G. 2020, GeoRL, 47, e2020GL088303
Zeng, L., Jacobsen, S. B., Sasselov, D. D., et al. 2019, PNAS, 116, 9723
Zhang, H.-W. 2007, AcMeS, 43, 113